An Ultrasonic Rangefinder Based on an AlN Piezoelectric Micromachined Ultrasound Transducer

Richard Przybyla,
Igor Izyumin, Mitchell Kline, Bernhard Boser
Berkeley Sensor and Actuator Center
University of California, Berkeley
Berkeley, California 94720
Email: rjp@berkeley.edu

Stefon Shelton,
André Guedes, David Horsley
Berkeley Sensor and Actuator Center
University of California, Davis
Davis, California 95616

***Abstract*—An ultrasonic rangefinder has a working range of 30 mm to 450 mm and operates at a 375 Hz maximum sampling rate. The worst-case systematic error less than 1.1 mm. The rms noise is proportional to the square of the distance and equals 1.3 mm at the maximum range. The range measurement principle is based on pulse-echo time of flight measurement using a single transducer for transmit and receive consisting of a piezoelectric AlN membrane with 400 μm diameter which was fabricated using a low-temperature process compatible with processed CMOS wafers. All circuits are low voltage, enabling integration in standard low voltage circuit technology.**

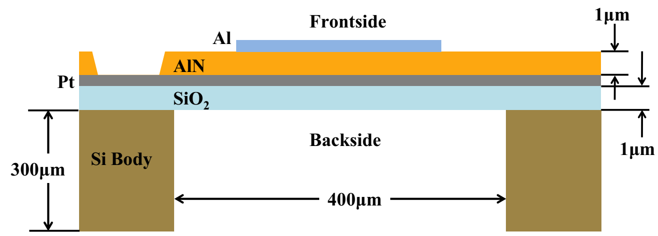

Fig. 1. Cross-section of pMUT.

I. Introduction

Ultrasonic sensors have many applications including imaging, rangefinding for computer vision, human machine interaction, short-range navigation, non-destructive testing, and flow sensing. Ultrasonic rangefinding is an attractive alternative to radio frequency- and light-based rangers at short ($<$10 m) distances since the relatively low speed of sound alleviates the high speed electronics requirements of optical solutions.

However, commercially available bulk piezoelectric transducers suffer from a high acoustic impedance mismatch to air, which results in poor transduction efficiency between the electrical and acoustical domains. The addition of special materials to the transducer surface can improve the efficiency, but work only in a limited bandwidth. While capacitive micromachined ultrasound transducers (cMUTs) [1], [2] circumvent these problems by miniaturizing the transducer using integrated circuit technology, they require high bias voltages and complicated fabrication processes. Piezoelectric micromachined ultrasound transducers (pMUTs) [3], [4] do not need a bias and need are much simpler to fabricate. In addition, the aluminum nitride (AlN) piezoelectric layer used in this work [5] is readily integrable with foundry CMOS, enabling fully integrated solutions with on-chip signal processing. This is particularly attractive in applications requiring multiple transducers for beam forming and imaging.

Ultrasonic rangefinders operate either in continuous wave (CW) mode or pulse-echo (PE) mode. Narrowband CW systems [6] suffer from multipath fading that can cause large range errors. Frequency modulated continuous wave (FMCW) excitation can overcome multipath fading [7], but requires very high dynamic range since the transmitted signal dwarfs the return signal. PE excitation has lower average output power compared to CW but the transmit pulse and return echoes are separated in time, thereby avoiding the dynamic range and multipath problems that plague CW systems.

In this work, we present a model for the pMUT and the acoustic channel which includes electrical, mechanical, and acoustic domains. The model, presented in Section II, is the basis for a pulse-echo ultrasonic rangefinder design based on a single pMUT, which is presented in Section III. The device operates over a working range of 30 mm - 450 mm. The measurement error consists of a random component dominated by noise sources in the transducer and a systematic error caused by the range ambiguity that results from the divergence of the beam. The random error increases quadratically with distance and is 1.3 mm at 450 mm. The range ambiguity for a large flat target is periodic and has a peak value of 1.1 mm.

II. Theory and Characterization Data

A. Device Structure

The ultrasound transducer [5] consists of a unimorph membrane with diameter 400 μm consisting of an SiO_2/Pt/AlN/Al sandwich fabricated on a Si wafer. As Figure 1 shows, a trench etched though the wafer exposes both sides of the membrane. The electrical field resulting from a voltage applied between the Al and Pt electrodes results in a transverse stress in the AlN layer and consequent out-of-plane bending of

This material is based upon work supported by the Defense Advanced Research Projects Agency (DARPA) and/or the Space and Naval Warfare Center, San Diego (SPAWAR SSC-SD) under Contract No. N66001-08-C-2023

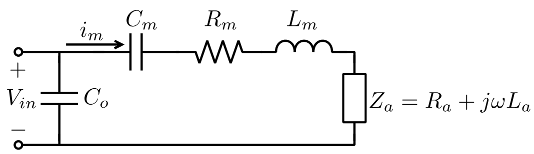

Fig. 2. Electrical model of transducer.

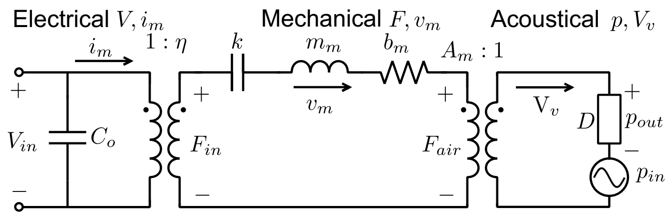

Fig. 3. Electrical, mechanical, and acoustical model of ultrasound transducer.

the membrane which produces a pressure wave. Similarly, an incident pressure wave results in membrane deformation and consequent charge on the electrodes enabling the device to be used both as a transmitter and receiver.

B. Transducer Electromechanical Model

For small displacements of less than approximately 0.6 μm the membrane behaves like a linear resonator. Figure 2 shows an electrical equivalent model. In this model, capacitor C_m models the equivalent lumped membrane stiffness, L_m the mass, and R_m the loss to the substrate. Impedance Z_a represents the interface to the air. The resistive part R_a models the acoustic power delivered to or received from the air. The values of C_o, C_m, $R_p = R_m + R_a$, and $L_p = L_m + L_a$, as well as the resonant frequency f_o and the quality factor Q can be determined with a network analyzer and are listed in Table I.

The electrical model accurately reflects the characteristics of the transducer at its electrical port, but only indirectly describes its mechanical and acoustic properties. Figure 3 shows a refined model where all domains are represented explicitly and coupled with ideal transformers. In this model all components are represented by electrical equivalents. Voltage and current correspond to force and membrane velocity v_m in the mechanical domain and pressure and volume velocity $\mathrm{V}_v = v_m A_m$ in the acoustic domains, respectively, where A_m is the effective area of the membrane.

The coupling coefficient $\eta = F_{in}/V_{in}$ between the electrical and mechanical domains can be determined from a measurement of the proof mass displacement at resonance, $x(\omega_o)$ using a Laser Doppler Vibrometer (LDV). At resonance, the voltage across capacitor C_m equals QV_{in}, and the force on the spring k is $kx(\omega_o)$, thus $\eta Q V_{in} = kx(\omega_o)$. Using $k = \eta^2/C_m$ yields

$$\eta = \frac{QV_{in}C_m}{x(\omega_o)}. \tag{1}$$

The mechanical force on the air, F_{air}, estblishes a pressure difference $p_{air} = F_{air}/A_m$ between the front- and backside of the membrane. In the model, D represents the acoustic

TABLE I
VALUES OF VARIOUS PARAMETERS AT RESONANCE

Description	Electrical	Mechanical	Acoustical
Stiffness	C_m : 82.34 fF	k : 500 N/m	—
Membrane mass	L_m : 6.1 H	m_m : 35 ng	—
Acoustic mass	L_a : 0.62 H	m_a : 25 ng	$Im(D)$: 2000 $\frac{\mathrm{Rayls}}{\mathrm{mm}^2}$
Substrate damping	R_m : 385 kΩ	b_m : 16 $\frac{\mu\mathrm{Ns}}{\mathrm{m}}$	—
Air damping	R_a : 69 kΩ	b_a : 2.8 $\frac{\mu\mathrm{Ns}}{\mathrm{m}}$	$Re(D)$: 920 $\frac{\mathrm{Rayls}}{\mathrm{mm}^2}$
Coupling Ratio	—	η : 6.4 $\frac{\mu\mathrm{N}}{V}$	A_m : 0.038 mm^2
Feedthrough	C_o : 14.6 pF	—	—
Resonant Frequency	f_o : 214 kHz		
Quality Factor	Q : 20		

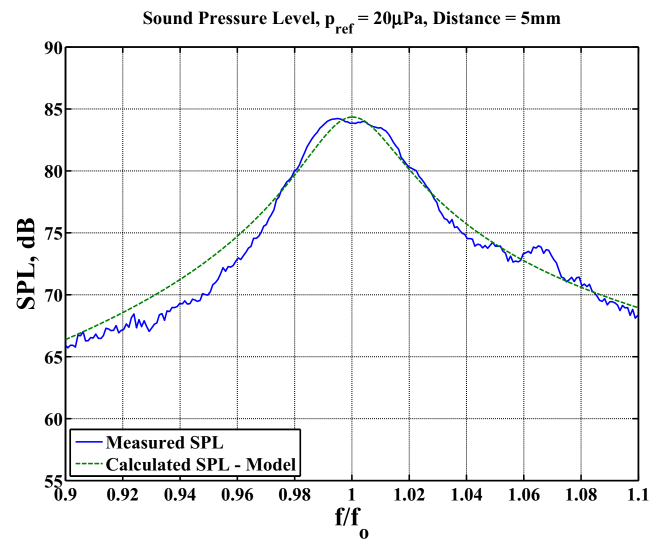

Fig. 4. SPL vs. normalized frequency from measurement and theory.

impedance of the air, $D = p_{air}/V_v$ and is given by [8]

$$D = \frac{\rho c}{A_m}\left(1 - \frac{2J_1(2wa)}{2wa} + j\frac{2K_1(2wa)}{2wa}\right), w = \frac{4\pi}{\lambda} \tag{2}$$

In this equation, ρ is the density of air, $\lambda \approx 1.6$ mm is the wavelength of sound at f_o, J_1 is the first order Bessel function, K_1 is the first order Struve function, and a is the effective radius of the membrane. Since the membrane radius is smaller than the wavelength, the real part of the term in the parentheses is less than unity, resulting in a somewhat reduced effective impedance of the air, R_a. Although this decreases the mechanical efficiency to 15%, the transduction efficiency of the device is still significantly higher than that of bulk piezoelectrics [9]. Table I summarizes the measured device parameters which result in a conversion factor at resonance $s_{out} = p_{out}/V_{in}$ =26 Pa/V and short-circuit current sensitivity $s_i = i_m/p_{in}$ =13 nA/Pa.

C. Return Echo Attenuation

In a rangefinder, the echo signal strength depends on the target distance and acoustic reflectivity. The latter is near unity since for most materials the acoustic impedance is

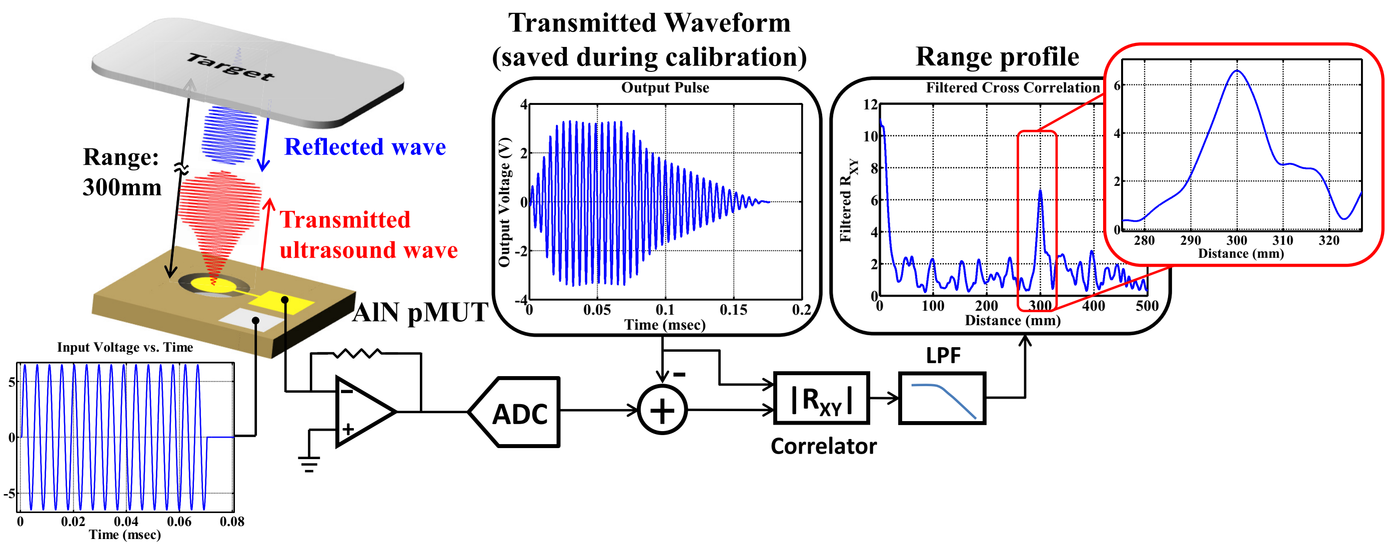

Fig. 5. Block diagram of rangefinder.

several orders of magnitude larger than that of air. Since $\lambda \gg a$ at resonance for the transducer described here, the ultrasound energy radiates isotropically from the frontside of the transducer, resulting in a linear attenuation of pressure with distance. Additionally, the vibration of the air molecules give rise to an exponential signal attenuation [10]. Assuming perfect target reflectivity, the ratio of the received to the transmitted pressure is

$$G_{ch} = \frac{p_{in}}{p_o} = \frac{\sqrt{A_m}}{4\sqrt{\pi}R_T}10^{-2\alpha R_T}, \tag{3}$$

where $\alpha = 3.61 \times 10^{-6} f - 0.0985$ is the attenuation constant in bels/meter, and f is the frequency of the sound wave. For example, at $R_T = 400\,\mathrm{mm}$ and $f = 200\,\mathrm{kHz}$, the attenuation is $p_{in}/p_o = -83\,\mathrm{dB}$. The linear term dominates up to approximately 1m. At 400 mm, the exponential term contributes $-10\,\mathrm{dB}$.

Because of the funnel created by the through-wafer hole below the membrane, the radiation out of the backside of the transducer is not exactly isotropic. Because of the higher concentration of radiated power in the direction perpendicular to the membrane, the attenuation in this direction is less than predicted by the equation stated above. The measured improvement is 17.1 dB. In rangefinder applications the narrower radiation pattern from the backside has two advantages: The larger return signal improves the signal-to-noise ratio and hence maximum range of the system. In addition, the better focus reduces the error caused by target range ambiguity.

D. Model Verification with Acoustic Test

To verify the model, the pMUT is driven near resonance with $V_{in} = 400\,\mathrm{mV}_{rms}$ and the acoustic output measured with a high frequency microphone mounted 5 mm from the front surface of the pMUT. Figure 4 compares the measured sound pressure level (SPL) to the prediction from the model and shows excellent agreement.

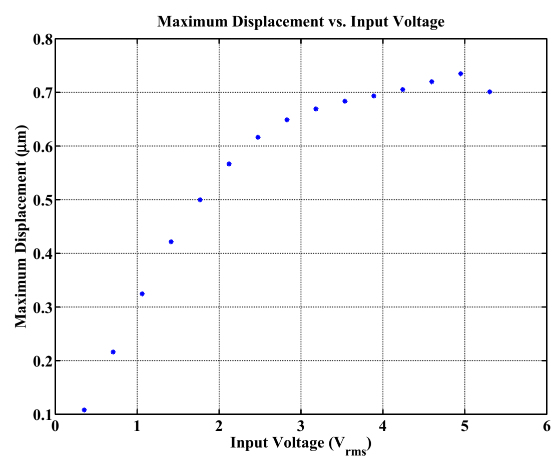

Fig. 6. Membrane displacement as a function of drive voltage V_{in} at resonance.

III. RANGEFINDER

The transducer described above is used in the acoustic pulse-echo rangefinder shown conceptually in Figure 5. The pMUT is excited with 15 cycles of a V_{in} =4.2 V rms sinusoid at its resonant frequency f_o resulting in an acoustic burst being emitted and reflected at the target. The backside of the transducer is used to realize the benefits discussed above.

A transimpedance amplifier measures current (which is proportional to the membrane velocity) resulting from the acoustic echo. The target distance R_T is then calcuated from the delay $\tau = 2R_T/c$ and the speed of sound, c.

A simple implementation would use short pulses with a well defined start to measure range. In practice, such pulses

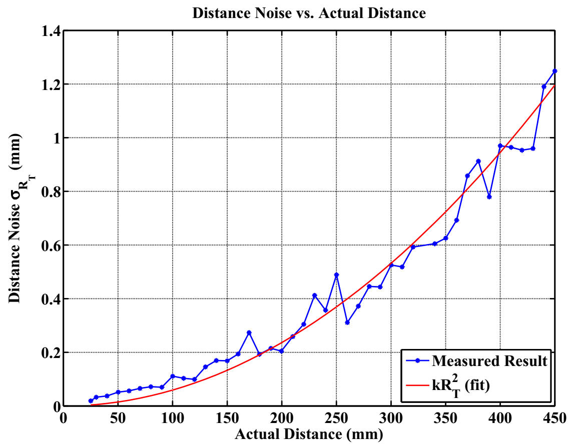

Fig. 7. Random distance noise versus target range R_T.

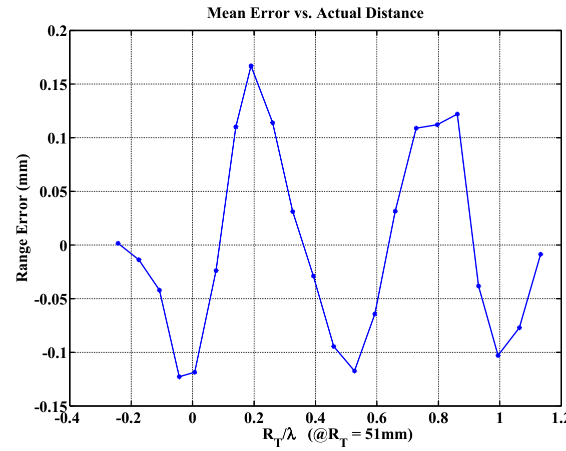

Fig. 8. Systematic error due to finite beam width.

would be signficiantly distorted by the narrow-band response of the transducer and limited to very low power. These problems are avoided by exciting the transducer with a short sinusoidal burst (15 cycles) at the resonant frequency. This choice represents a compromise between transmit power and pulse duration which sets the minimum range. Figure 6 shows the peak amplitude of the transmit pulse as a function of drive amplitude V_{in}. By driving the system in the nonlinear region the signal power and hence maximum range can be increased substantially. This requires, however, that the transmit pulse decays and the system to returns to the linear regime before the echo is received. The resulting transmitted wave is shown in Figure 5. The clipping at high amplitude due to nonlinearity as well as the ring-up and long tail that are the result of the high-Q response of the transmitter are clearly visible. At short range, the tail overlaps and corrupts the received echo resulting in measurement errors. To supress this error, the transmitted waveform is measured during a calibration phase and subsequently subtracted from the transducer output, as indicated in the block diagram.

The round trip delay τ is determined from correlating the corrected return echo with the transmit pulse. Since the transmit pulse is narrowband with bandwidth $B \approx f_o/Q$, the correlator acts as a matched filter that rejects broadband noise. The resulting improved signal-to-noise ratio greatly increases the maximum operating distance of the rangefinder.

Figure 5 shows the resulting range profile for a sample target distance of $R_T = 300\,\text{mm}$. The strong peak at zero range is due to imperfect cancellation of the transmit pulse and limits the minimum useful range to 30 mm.

The periodicity of the transmit signal results in a $\pm\lambda/2$ periodicity of the correlation, resulting in a corresponding error in the range estimate. A linear averaging filter at the correlator output reduces its value. The remaining error is dominated by thermal noise from the transducer and the interface circuits and has an approximately Gaussian distribution.

Figure 7 shows the measured random noise as a function

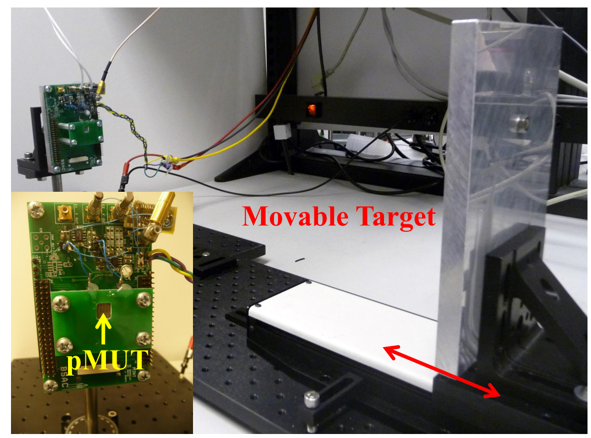

Fig. 9. Experimental setup. Inset shows prototype circuit board with pMUT mounted with backside facing target.

of target range. It increases quadratically with distance due to increased signal attenuation as predicted by Equation 3 in the regime where linear signal attenuation dominates. The dominant noise sources are the mechanical and acoustic damping in the transducer modeled by the Johnson noise from R_m and R_a in the transducer model, as well as noise from the transresistance amplifier. Lowering C_o reduces the amplifier noise gain and hence its contribution to the overall noise.

The spatial divergence of the transmitted beam introduces uncertainty in the distance measurement that depends on the shape of the target. The received echo is the superposition of signals with (slightly) different delays. Figure 8 shows the resulting error for a flat target. The error is a function of distance and has periodicity of approximately $\lambda/2$, and it has a peak value of 1.1 mm. Its value can be reduced by decreasing the beam width, e.g. by using an array of transducers.

The temperature dependence of the speed of sound adds an additional error of $0.2\,\%/^o$C. Its effect can be reduced with temperature compensation.

The prototype rangefinder was tested using a moving stage with a metal target. Figure 9 shows the experimental setup. The rangefinder has a working range of 30 mm to 450 mm. No averaging is used; the sample rate is limited to 375Hz by the round-trip delay of 2.6 ms at the maximum range at room temperature.

IV. Conclusion

Piezoelectric micromachined ultrasound transducers enable compact and low power near field ranging with millimeter or better accuracy. Unlike capacitive transducers, no high-voltage bias is required and the unimorph design leads to a very simple manufacturing process. The thin membrane structure enabled by Aluminum Nitride results in significantly improved coupling to air compared to published results fabricated with bulk PZT. Using a single device for both transmit and receive reduces complexity and alleviates problems from frequency mismatch but introduces range ambiguity due to beam divergence. This problem could be overcome with arrays of devices.

References

[1] I. Ladabaum, X. Jin, H. Soh, A. Atalar, and B. Khuri-Yakub, "Surface micromachined capacitive ultrasonic transducers," *Ultrasonics, Ferroelectrics and Frequency Control, IEEE Transactions on*, vol. 45, no. 3, pp. 678 –690, May 1998.

[2] I. Wygant, M. Kupnik, J. Windsor, W. Wright, M. Wochner, G. Yaralioglu, M. Hamilton, and B. Khuri-Yakub, "50 kHz capacitive micromachined ultrasonic transducers for generation of highly directional sound with parametric arrays," *Ultrasonics, Ferroelectrics and Frequency Control, IEEE Transactions on*, vol. 56, no. 1, pp. 193 –203, Jan. 2009.

[3] J. Bernstein, S. Finberg, K. Houston, L. Niles, H. Chen, L. Cross, K. Li, and K. Udayakumar, "Micromachined high frequency ferroelectric sonar transducers," *Ultrasonics, Ferroelectrics and Frequency Control, IEEE Transactions on*, vol. 44, no. 5, pp. 960 –969, Sept. 1997.

[4] P. Muralt, N. Ledermann, J. Paborowski, A. Barzegar, S. Gentil, B. Belgacem, S. Petitgrand, A. Bosseboeuf, and N. Setter, "Piezoelectric micromachined ultrasonic transducers based on pzt thin films," *Ultrasonics, Ferroelectrics and Frequency Control, IEEE Transactions on*, vol. 52, no. 12, pp. 2276 –2288, Dec. 2005.

[5] S. Shelton, M.-L. Chan, H. Park, D. Horsley, B. Boser, I. Izyumin, R. Przybyla, T. Frey, M. Judy, K. Nunan, F. Sammoura, and K. Yang, "CMOS-compatible AlN piezoelectric micromachined ultrasonic transducers," in *Ultrasonics Symposium (IUS), 2009 IEEE International*, Oct 20-23 2009, pp. 402 –405.

[6] C. Kuratli and Q. Huang, "A CMOS ultrasound range-finder microsystem," *Solid-State Circuits, IEEE Journal of*, vol. 35, no. 12, pp. 2005 –2017, Dec. 2000.

[7] S. Roehr, P. Gulden, and M. Vossiek, "Precise distance and velocity measurement for real time locating in multipath environments using a frequency-modulated continuous-wave secondary radar approach," *Microwave Theory and Techniques, IEEE Transactions on*, vol. 56, no. 10, pp. 2329 –2339, Oct. 2008.

[8] D. T. Blackstock, *Fundamentals of Physical Acoustics*. John Wiley & Sons, 2000.

[9] M. Haller and B. Khuri-Yakub, "1-3 composites for ultrasonic air transducers," in *Ultrasonics Symposium, 1992. Proceedings., IEEE 1992*, vol. Vol.2, Oct 1992, pp. 937–939.

[10] L. B. Evans and H. E. Bass, "Tables of absorption and velocity of sound in still air at 68F," Wyle Labratories, Tech. Rep. Report WR72-2., Jan. 1972.